FULL PAPER

Magnetic Resonance in Medicine 00:00–00 (2014)

Short-T_2 Imaging for Quantifying Concentration of Sodium (^{23}Na) of Bi-Exponential T_2 Relaxation

Yongxian Qian,[1,2]* Ashok Panigrahy,[3] Charles M. Laymon,[4] Vincent K. Lee,[3] Jan Drappatz,[5] Frank S. Lieberman,[5] Fernando E. Boada,[6] and James M. Mountz[4]

Purpose: This work intends to demonstrate a new method for quantifying concentration of sodium (^{23}Na) of bi-exponential T_2 relaxation in patients on MRI scanners at 3.0 Tesla.

Theory and Methods: Two single-quantum (SQ) sodium images acquired at very-short and short echo times (TE = 0.5 and 5.0 ms) are subtracted to produce an image of the short-T_2 component of the bi-exponential (or bound) sodium. An integrated calibration on the SQ and short-T_2 images quantifies both total and bound sodium concentrations. Numerical models were used to evaluate signal response of the proposed method to the short-T_2 components. MRI scans on agar phantoms and brain tumor patients were performed to assess accuracy and performance of the proposed method, in comparison with a conventional method of triple-quantum filtering.

Results: A good linear relation ($R^2 = 0.98$) was attained between the short-T_2 image intensity and concentration of bound sodium. A reduced total scan time of 22 min was achieved under the SAR restriction for human studies in quantifying both total and bound sodium concentrations.

Conclusion: The proposed method is feasible for quantifying bound sodium concentration in routine clinical settings at 3.0 Tesla. **Magn Reson Med 000:000–000, 2014. © 2014 Wiley Periodicals, Inc.**

Key words: sodium MRI; bound sodium imaging; short-T_2 sodium imaging; sodium quantification; brain tumor

INTRODUCTION

Sodium ions (Na^+) in human body are either in fast and free motion in fluids (blood and cerebrospinal fluid, CSF), or in slow and restricted motion in cells and tissues due to binding to macromolecules such as intracellular proteins and extracellular matrix (1–6). Concentration of bound sodium is tightly regulated in normal cells and tissues but not properly regulated in abnormal ones such as cancer cells and degenerative cartilages (4, 6, 7). Noninvasive measurement of bound sodium concentration has the potential to establish an endogenous imaging biomarker for detecting early pathological changes in a wide range of conditions and diseases, from cartilage degeneration to brain tumors and neurological disorders such as bipolar, epilepsy, concussion, and others.

MRI quantification of the bound sodium (^{23}Na) is based on its unique bi-exponential decay of transverse (T_2) relaxation, with 60% of total intensity for the short- and 40% for the long-T_2 components (8–11). The bi-exponential decay results from electrical and dynamic micro-environment around spins. A sodium nucleus has electric quadrupole and spin 3/2 (12, 13). The electric quadrupole moment interacts with electric field gradient at sodium binding site and generates four degenerative energy states (or levels): 3/2, 1/2, −1/2, and −3/2. Transitions between the energy levels produce single-, double-, or triple-quantum coherences. A 90°-radiofrequency (RF) pulse excites the spins and produces single-quantum (SQ) coherences from transitions between the outer levels (3/2 → 1/2; −1/2 → −3/2) and between the inner levels (1/2 → −1/2). The outer-level SQ transverse relaxation has an exponential decay, $exp\ (-t/T_{2S})$, faster than the inner one, $exp\ (-t/T_{2L})$, with $T_{2L} > T_{2S}$ (8, 14). The two exponential decays degenerate to one decay with a T_2 time larger than T_{2L} (14), if sodium nuclei are in free motion or move very fast (i.e., motion correlation time among sodium nuclei is much shorter than the inverse of Larmor frequency, $\tau_c << 1/\omega_0$). A series of 90°-RF pulses generates double- or triple-quantum coherences from transitions between the nonadjacent energy levels, which are selectively detectable by means of phase cycling (15–17) or pulsed field gradients (18). These multiple-quantum coherences are used to detect bound sodium in slow motion by means of the bi-exponential decay. Triple-quantum filtering (TQF) has been used for this purpose more frequently than double-quantum filtering due to its 50% higher signal output (19). It is worth mentioning that bound sodium gives rise to the bi-exponential decay regardless of whether the sodium is intra- or extracellular.

The TQF imaging, when used for patient studies in clinical setting, is facing three major challenges. The first is the low signal-to-noise ratio (SNR) because triple-quantum (TQ) signal is approximately 10% of corresponding single-quantum signal (20–22). The second is

[1]MR Research Center, Department of Radiology, University of Pittsburgh, Pittsburgh, Pennsylvania, USA.
[2]Department of Bioengineering, University of Pittsburgh, Pittsburgh, Pennsylvania, USA.
[3]Department of Radiology, Children's Hospital of Pittsburgh of UPMC, Pittsburgh, Pennsylvania, USA.
[4]PET Center, Department of Radiology, University of Pittsburgh, Pittsburgh, Pennsylvania, USA.
[5]Department of Neurology and Medicine, University of Pittsburgh, Pittsburgh, Pennsylvania, USA.
[6]Department of Radiology, New York University, New York, New York, USA.

Grant sponsor: NIH; Grant number: U01 CA140230; Grant sponsor: Children's Hospital of Pittsburgh Foundation and Ian's Friends Foundation; Grant sponsor: the Department of Radiology Development Fund, University of Pittsburgh.

*Correspondence to: Yongxian Qian, Ph.D., 200 Lothrop Street, PUH B804, Pittsburgh, PA 15213. E-mail: qiany@upmc.edu or qiany@glabscloud.com

Received 10 April 2014; revised 13 June 2014; accepted 10 July 2014
DOI 10.1002/mrm.25393
Published online 00 Month 2014 in Wiley Online Library (wileyonlinelibrary.com).

the high specific absorption rate (SAR) that results in long acquisition time (~40 min) to meet the SAR constraints on humans. Such a long acquisition time is difficult to tolerate by patients. The third challenge is the heavy dependence of TQ signal on T_2 times of both short- and long-T_2 components, limiting TQF imaging to the detection, rather than quantification, of bound sodium (22, 23).

To address these challenges alternative approaches have been proposed. The inversion recovery (IR) approach, adopted from proton (^{1}H) MR imaging, was proposed to highlight bound sodium signal by suppressing free sodium signal from fluid (24). It takes advantage of the difference in T_1 relaxation of sodium in tissues, such as in human brain where T_1 is 20–40 ms in CSF, ~17 ms in white matter, and ~11 ms in gray matter at 1.5T (25). Although the IR approach significantly reduces RF power and completely suppresses unwanted fluid signal (26, 27), it is not suitable for quantification of bound sodium due to concurrent partial suppression of tissue signals. In addition, the IR pulse still has significant SAR-related limitations on total scan time. Low amplitude and long duration (~10 ms) IR pulses may ameliorate this difficulty (26).

Another alternative approach was recently proposed, in which a bi-exponential-decay-related sodium image was attained by subtracting an SQ image acquired at a long echo time (11 ms) from a spin-density-weighted image acquired at a very short echo time (0.3 ms) (28). This approach increases SNR by up to 3-folds over the TQF imaging, but it does not reduce the SAR as it still requires three RF pulses for excitation. A version of this sequence with two RF pulses has been proposed to ease the SAR issue (29).

In this work, we propose a new approach that simultaneously addresses the three challenges (SAR, SNR and quantification) faced by the TQF approach. Our method, referred to as the short-T_2 imaging, detects bound sodium through short-T_2 component by subtracting two SQ sodium images acquired at very-short (0.5 ms) and short (5.0 ms) echo times. As a single RF pulse is used for each SQ image, the SAR limitation is mitigated. Signal intensity from the short-T_2 component is approximately 60% of the SQ signal, and thus the new method has the potential to increase SNR by 6-folds over the TQF approach. More importantly, it can quantify the concentration of bound sodium as it has a nearly-uniform signal response to both short and long T_2 relaxations in the range of interest.

The subtraction methodology, although widely used in proton (^{1}H) MR imaging (30), was first proposed in sodium (^{23}Na) MR imaging by Hilal et al (31, 32). However, their method is different from ours in the design in which our goal is to achieve a uniform response to all the T_2 components of interest for the quantification of bound sodium concentration.

THEORY

Signal Model

A two-compartment model is proposed here to describe single-quantum sodium signal in a voxel: bound and free sodium. In the compartment of bound sodium, T_2 relaxation decays bi-exponentially with short- and long-T_2 times of $T_{2b,S}$ and $T_{2b,L}$. In the compartment of free sodium, T_2 relaxation decays mono-exponentially with a long T_2 time of T_{2fr}. The total signal in a voxel of unit volume is described by the following equation.

$$s(t) = V_b C_b \eta_b [a_{b,S} \exp(-t/T_{2b,S}) + a_{b,L} \exp(-t/T_{2b,L})] + V_{fr} C_{fr} a_{fr} \eta_{fr} \exp(-t/T_{2fr}) + n(t). \quad [1]$$

In Eq. [1], V is volumetric fraction (percentage) of a compartment and C is sodium concentration. a is intensity fraction of a T_2 component, with $a_{b,S} + a_{b,L} = 1$. $\eta = 1 - \exp(-TR/T_1)$ is saturation factor related to T_1 relaxation in a compartment at a repetition time of TR. It is known that sodium T_1 relaxation also decays bi-exponentially. However, the short-T_1 component is approximately 20% of total intensity and is usually ignored in imaging practice (14, 22). $n(t)$ is random noise of Gaussian distribution $N(0,\ \sigma^2)$.

Short-T_2 Sodium Image

The short-T_2 sodium image is defined here as the subtraction between two single-quantum sodium images acquired at very short (TE_1) and short (TE_2) echo times, respectively. Based on the Eq. [1], the short-T_2 sodium image, $s_{T2,S}$, is described as:

$$s_{T2,S} \equiv s(TE_1) - s(TE_2) = V_b C_b \eta_b (a_{b,S} \delta_{b.S} + a_{b,L} \delta_{b,L}) + V_{fr} C_{fr} \eta_{fr} a_{fr} \delta_{fr} + \delta_n, \quad [2a]$$

$$\text{where } \delta_n \equiv n(TE_1) - n(TE_2) \sim N(0, 2\sigma^2), \quad [2b]$$

$$\delta_{b,S} \equiv \exp(-TE_1/T_{2b,S})[1 - \exp(-\Delta TE/T_{2b,S})], \quad [2c]$$

$$\delta_{b,L} \equiv \exp(-TE_1/T_{2b,L})[1 - \exp(-\Delta TE/T_{2b,L})], \quad [2d]$$

$$\delta_{fr} \equiv \exp(-TE_1/T_{2fr})[1 - \exp(-\Delta TE/T_{2fr})], \quad [2e]$$

where $\Delta TE = TE_2 - TE1$. When $TE_1 < TE_2 < T_{2b,L} < T_{2fr}$ and at typical T_2 relaxations in the brain (33–35), Eqs. [2a–e] yield

$$s_{T2,S} \approx V_b C_b \eta_b a_{b,S} \delta_{b,S} + \delta_n. \quad [2f]$$

Optimization of TE_1 and TE_2

To make the estimation of $s_{T2,S}$ in Eq. [2f] as accurate as possible, the residual quantities in Eqs. [2d], [2e] should be minimized by selecting an optimal TE_2 while keeping TE_1 as short as possible. This leads to

$$\max_{TE_1 < TE_2 < T_{2b,L}} \{\delta_{b,S}\} \text{ while } \min_{TE_1 < TE_2 < T_{2b,L}} \{\delta_{b,L}; \delta_{fr}\}. \quad [3a]$$

The optimal TE_1 and TE_2 should also make a uniform (or flat) response of $s_{T2,S}$ to a range of $T_{2b,S}$ and $T_{2b,L}$ values of interest, that is,

$$\min_{TE_1 < TE_2 < T_{2b,L}} \{s_{T2,S} - \text{constant}\}. \quad [3b]$$

For the optimization of TE_1 and TE_2, TR is also a key parameter but there is a limitation on adjusting TR due to SAR restriction.

Off-Resonance Correction (ORC)

The SQ images may suffer image blurring from a combination of long readout time and inhomogeneity of the main magnetic field B_0. Artificial changes in adjacent voxels may appear in the subtraction image which are not relevant to actual changes of bound sodium concentration. It is important to correct image blurring before the subtraction.

To correct image blurring, an accurate 3D B_0-field map, $\Delta B(r)$, or frequency map, $\Delta f(r) = \gamma\, \Delta B(r)$, is needed, where γ is gyromagnetic ratio in Hz/Tesla for sodium nuclei and $r = (x, y, z)$ is spatial coordinates of a voxel. The field map can be estimated by taking phase difference between the two TE-images, $m(r,\ TE_1)$ and $m(r,\ TE_2)$,

$$\Delta f(r) = phase[m(r,\ TE_2) \cdot m^*(r,\ TE_1)]/[2\pi(TE_2 - TE_1)]. \quad [4]$$

The function *phase*() takes the phase of its complex variable and the operator * performs conjugate operation. Phase wrapping is less likely happening in this estimate because of small gyromagnetic ratio of sodium nuclei. For instance, a phase change of π in 4.5 ms (=TE_2–TE_1) for sodium (^{23}Na) corresponds to 111 Hz offset in B_0 field, or 422 Hz for proton (^{1}H). This offset is very large, and may be only possible with air cavities and sinus regions. The estimated frequency map is then used to correct image blurring by means of the conjugate phase algorithm (36, 37), as described below with the acquired k-space data, $s(k)$, and corrected image, $\hat{m}(r)$.

$$\hat{m}(r) = \sum_j h[k(t_j)] \cdot s[k(t_j)] \cdot \exp\{2\pi[r \cdot k(t_j) + \Delta f(r) \cdot t_j]\} \cdot \Delta k_j. \quad [5]$$

$k(t_j)$ is trajectory in the k-space at a readout time t_j. $h(k)$ is 3D Hann window, the same as used in image reconstruction before the image blurring correction. Δk_j is volume element surrounding the sampling point in the k-space.

To accelerate the calculation in Eq. [5] by means of fast Fourier transformation (FFT), a time-segmentation algorithm is used. The k-space data, $s(k(t_j))$, are grouped, first in the spatial-frequency directions (k_x, k_y, k_z) and then in the time direction t_j at a constant time step, *tStep*. At each time step, a constant phase is applied to the field term in Eq. [5].

T_2^* Correction of the TE_2 Image

After the off-resonance correction, the TE_2 image may need extra correction for T_2^* decay during the time period between TE_1 and TE_2. The TE_2 image is weighted by T_2^* decay, rather than by T_2 decay, as spin echo is usually not applicable to sodium imaging. The T_2^* decay stems from both macroscopic and microscopic inhomogeneity of the B_0 field within a voxel and may change from scan to scan. Macroscopic inhomogeneity becomes substantial when subjects have pathological lesions in an imaging volume. To minimize fluctuation of the T_2^* decay across scans, the TE_2 image should be corrected from T_2^*-weighted to T_2-weighted. This can be accomplished with an empirical relation between T_2 and T_2^* (30),

$$1/T_2^* = 1/T_2 + \kappa\gamma|\Delta B_0| = 1/T_2 + \kappa|\Delta f|. \quad [6]$$

κ is a unitless constant depending on relative scale of the macroscopic inhomogeneity of the B_0 field compared with the voxel size and shape of spin density distribution within a voxel. When voxel size is small (e.g., 3.44 mm in this study), a good first-order approximation to κ is 0.5 (30). With the estimated field map in Eq. [4], the TE_2 image is then corrected by multiplying with a factor,

$$\tilde{m}(r,\ TE_2) = m(r,\ TE_2) \cdot \exp[\kappa|\Delta f(r)| \cdot (TE_2 - TE_1)]. \quad [7]$$

Quantification of Bound Sodium Concentration

Accurate quantification of bound sodium concentration is difficult due to lack of measurement of volumetric fraction in a voxel. We quantify instead volume-fraction weighted bound sodium concentration (vBSC), C_{vb}=V_bC_b. An integrated linear calibration on the short-T_2 image and TE_1 image is used to quantify the bound sodium concentration, as well as total sodium concentration (TSC), C_{total}.

$$C_{total} = C_{fr}\frac{I_{TE1} - \bar{I}_{noise,TE1}}{\bar{I}_{fr,TE1} - \bar{I}_{noise,TE1}}, \quad [8a]$$

$$C_{vb} = \frac{C_{fr}}{g \cdot a_{b,S}} \cdot \frac{I_{ST2} - \bar{I}_{noise,ST2}}{\bar{I}_{fr,TE1} - \bar{I}_{noise,ST2}}. \quad [8b]$$

C_{fr} is the known sodium concentration in a pure free sodium compartment, such as 145 mM in human cerebrospinal fluid (35). I_{TE1} is image intensity at a pixel on the TE_1 image and $\bar{I}_{noise,TE1}$ is the mean of image intensities in a noise-only region. $\bar{I}_{fr,TE1}$ is the T_1-saturation (η_{fr}) corrected mean of image intensities in a pure fluid region of known concentration C_{fr} on the TE_1 image. I_{ST2} is image intensity in real part at a pixel on the short-T_2 image while $\bar{I}_{noise,ST2}$ is the mean of real-part image intensities in a noise-only region. g is gain of the short-T_2 imaging over a range of short T_2 values of interest, which will be determined later in the results section.

The whole process for the short-T_2 sodium imaging is summarized in Figure 1.

METHODS

Pulse Sequence

The proposed short-T_2 sodium imaging requires pulse sequences capable of producing high SNR because random noise is increased by a factor of $\sqrt{2}$ after the subtraction. The twisted projection imaging (TPI) sequence is a good candidate for this purpose (38), which produces an isotropic 3D sodium image of the brain in a 10-min scan at 3 T and a high SNR of >40 in the CSF regions. This remarkable achievement in SNR is based on a long readout time of ~36 ms which may raise concern on image blurring of the short-T_2 component. This concern can be

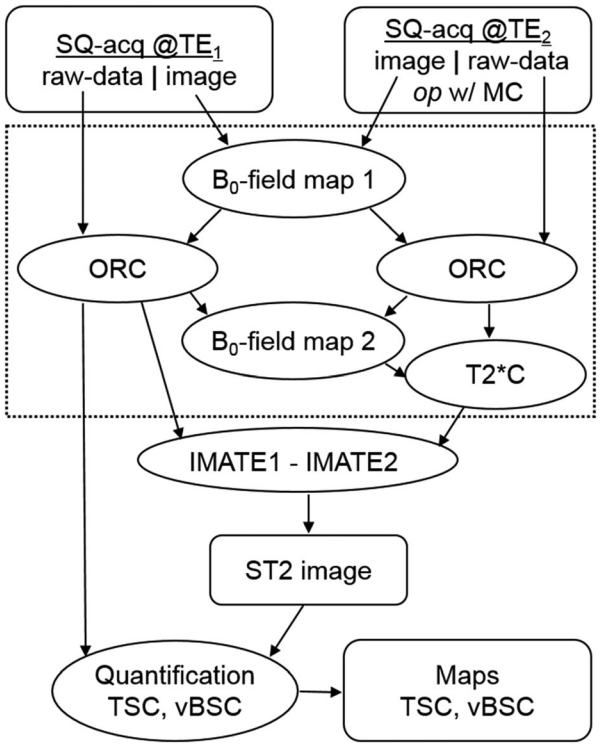

FIG. 1. Flowchart for the short-T_2 sodium imaging. SQ-acq: single-quantum data acquisition; op w/ MC: optional selection with motion correction; ORC: off-resonance correction; T2*C: T_2^* correction; IMATE1/TE2: image at TE_1/TE_2; TSC: total sodium concentration; vBSC: volume-fraction weighted bound sodium concentration. The processes in the dashed box are optional.

addressed by looking into the special design of TPI trajectory and its point spread function (PSF) as detailed below.

Image Blurring of the Short-T_2 Component

Image blurring was quantified for a short-T_2 component, a long-T_2 component, and a bi-component by means of the point spread function (PSF) of the TPI acquisition:

$$PSF(r) = \sum_j h[k(t_j)] \cdot [a_{21}\exp(-t_j/T_{21}^*) + a_{22}\exp(-t_j/T_{22}^*)] \cdot \exp\{2\pi[r \cdot k(t_j)]\} \cdot \Delta k_j, \quad [9]$$

where $k(t_j)$ is TPI trajectory in the 3D k-space at a readout time of t_j. $h(k)$ is 3D Hann window the same as used in the TPI image reconstruction. Δk_j is volumetric element surrounding a sampling point. The bi-component term will be replaced with mono-exponential term when the single-component is under investigation. Full width at half maximum (FWHM) of the PSF was used to quantify image blurring. A linear interpolation between pixels was used in the FWHM measurement. TE_1 and TE_2 are not included in Eq. [9], because they do not change with readout time. They scale magnitude but do not change shape of the TPI's PSF.

Phantoms

To validate quantification of the bound sodium, ten 50 mL centrifuge tube phantoms (90 mm length × 25 mm diameter) were custom-built with distilled water, 10% w/w agar powder, and NaCl at 10 different concentrations in a range of 15–150 mM. The 10% w/w agar provides sufficient binding sites for sodium ions at the high-end concentration (11, 39). The range of 15–150 mM simulates human brain tissues. To simulate free sodium in brain fluids, an extra tube phantom was built at 150 mM NaCl without agar. This saline water phantom also served as image quality control of the short-T_2 and TQF imaging. To measure spatial resolution of the short-T_2 imaging under the TPI acquisitions we used a larger cylindrical agarose phantom (120 mm length × 140 mm diameter) filled with 10% w/w agarose gel and 66.6 mM saline water.

Human Subjects

Seven patients with brain tumors of high grade gliomas including both anaplastic glioma (WHO III) and glioblastoma multiforme (GBM) (5 pediatric patients of age 12–23 years, and 2 adults of age 56–60 years), were investigated in this study which was approved by the IRB of the University of Pittsburgh. The consent forms were signed by the subjects or their parents.

MRI Scans

For the short-T_2 imaging, two single-quantum sodium images were acquired on a clinical 3T MRI scanner (Magnetom Trio Tim, Siemens Medical Solutions, Erlangen, Germany) with gradient amplitude of 40 mT/m and slew rate of 170 mT/m/ms. A dual-tuned (^{1}H-^{23}Na) volume head coil (Advanced Imaging Research, Cleveland, OH) was used for the B_0-field shimming by means of the ^{1}H channel and the sodium imaging by means of the ^{23}Na channel. Acquisition parameters of the TPI sequence for the phantoms and human subjects were the same: rectangular RF pulse of 0.8 ms duration (which was the minimum value available under the SAR restriction), flip angle = 80° (which was limited by SAR and TR), field of view (FOV) = 220 mm, matrix size = 64 (which led to a nominal isotropic resolution of 3.44 mm, i.e., 220 mm/64), TPI readout time = 36.32 ms, total TPI projections = 1596, $P = 0.4$, TR = 100 ms, $TE_1/TE_2 = 0.5/5$ ms, 4 averages, and total acquisition time per TE-image TA= 10 min 39 s.

The TQF imaging was only performed on the phantoms with a lower-resolution TPI trajectory: flip angle = 90°, FOV = 220 mm, matrix size = 64, TPI readout time = 36.16 ms, total TPI projections = 204, $P = 0.2$, 4 averages, three rectangular RF pulses of 1.0 ms duration for each pulse, preparation time $\tau = 3.0$ ms, evolution time $\delta = 0.1$ ms, TE = 4.0 ms, TR = 312 ms at SAR = 100%, phase cycling steps = 6 (initial phase = 30° and phase step = 60°), and TA = 25 min 28 s. The preparation time τ and echo time TE were optimized by means of a real-time calibration process, respectively.

Measurement of Spatial Resolution

Actual spatial resolution in the single-quantum or short-T_2 image was measured directly on the images (40). The width, d, of the image intensity decay along the diameter

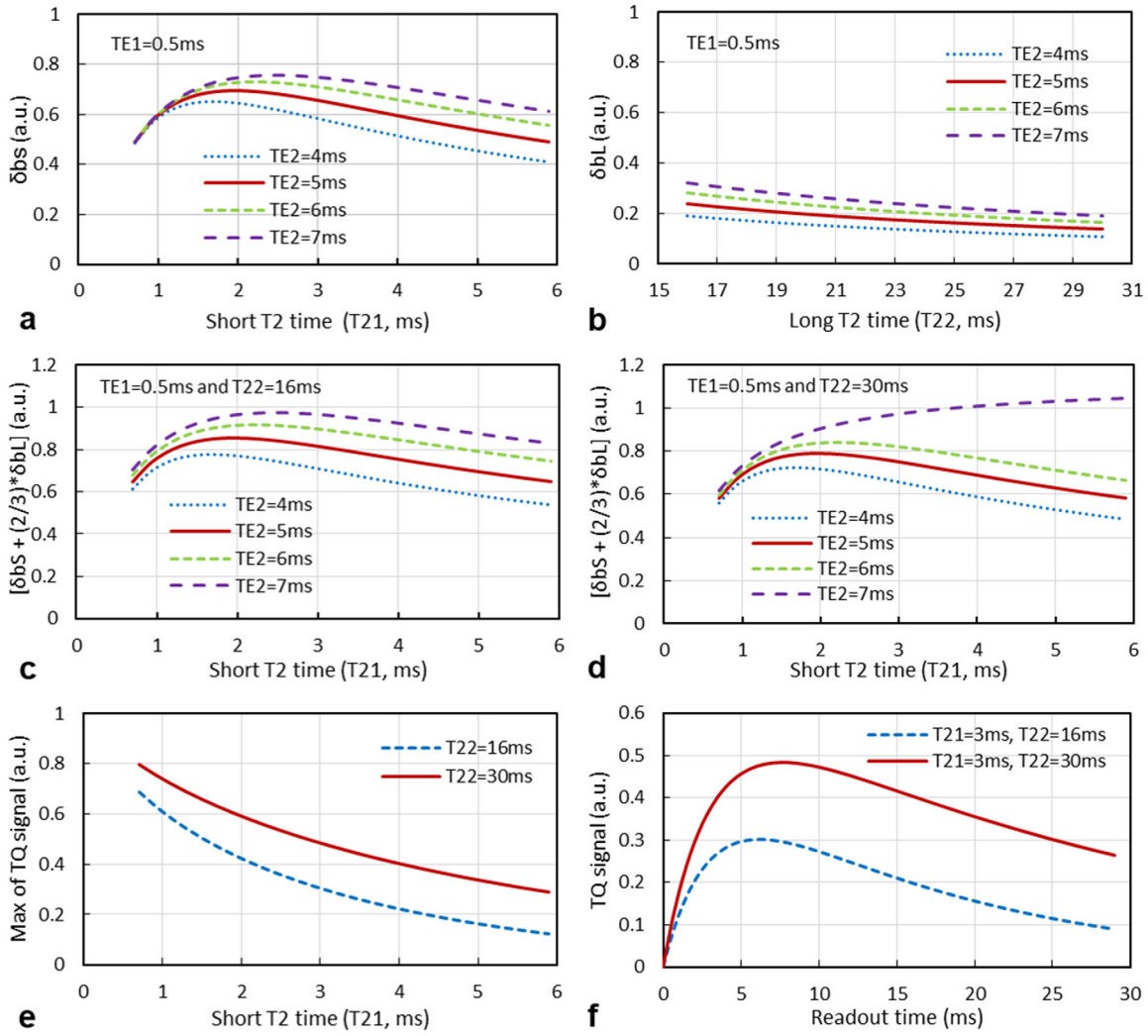

FIG. 2. Simulated signal response of the short-T_2 imaging: single component of short T_2 time (**a**), single component of long T_2 time (**b**), two components of a long T_2 time at low-end (**c**), and two components of a long T_2 time at high-end (**d**). **e**: Signal response of TQF imaging. **f**: Two of TQF signals used in e. A nearly-flat signal response is achieved in the short-T_2 imaging at $TE_1 = 0.5$ ms and $TE_2 = 5$–6 ms (red lines in c, d), but not achieved in the TQF imaging (e). [Color figure can be viewed in the online issue, which is available at wileyonlinelibrary.com.]

at the edge of the large agarose phantom was measured at its half way down to the bottom. The top and bottom of an edge were determined by averaging image intensity along their flat portions, respectively. The width was an estimate of the actual spatial resolution defined by the full width at half maximum (FWHM) of point spread function (40–43). This estimate is accurate when PSF is a triangle function. The measured resolution, slightly larger than the nominal resolution defined by the sampling in the k-space, consists of contributions from entire imaging process including B_0-field inhomogeneity, T_2^* decay, and filtering during image reconstruction.

Measurement of SNR

Because a quadrature volume head coil was used in this study, SNR was directly measured on the magnitude images (40, 44) by means of the following equations:

$$SNR = A/\sigma, \quad [10a]$$

$$A = \sqrt{(M_{\text{avg}})^2 - \sigma^2} \text{ for } A > 2\sigma, \quad [10b]$$

$$\sigma = M_{\text{avg}}(0)/1.25. \quad [10c]$$

M_{avg} (or $M_{\text{avg}}(0)$) is the mean of magnitude image intensity in a signal (or noise-only) region of interest. A is the mean signal amplitude in the signal region of interest and σ is the noise standard deviation in the real or imaginary part of the original complex image.

Quantification of Sodium Concentrations

Quantification was performed for both total and bound sodium concentrations. The TSC was calculated by means of Eq. [8a] on the SQ-image at TE_1. The vBSC was computed by means of Eq. [8b] on the short-T_2 image with an intensity fraction of $a_{b,S} = 0.6$ and a gain of $g = 0.76$ (which was determined in the Results Section below). The noise-only image intensity, $\bar{I}_{noise}$, was measured on the SQ and short-T_2 image, respectively.

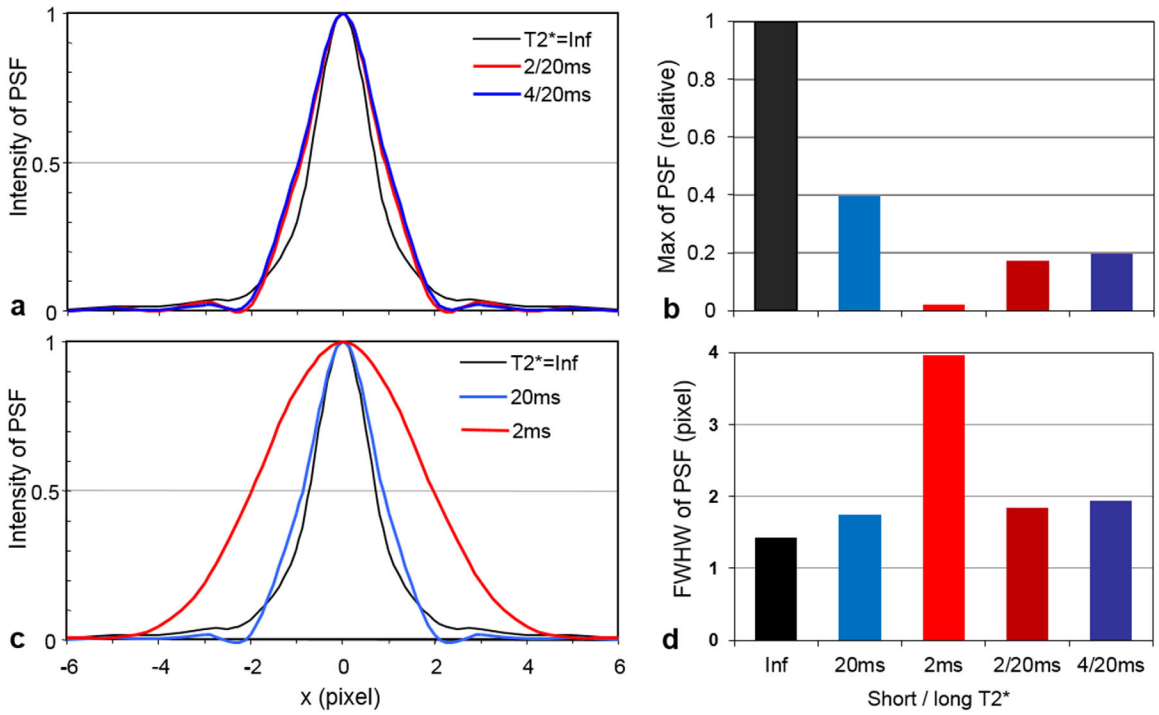

FIG. 3. Point spread function (PSF) of the TPI acquisition on bi-exponential T_2^* decay (**a**) and mono-exponential T_2^* decay (**c**), compared with no T_2^* decay ($T_2^* = \text{Inf}$). The maximum intensity and full-width-at-half-maximum (FWHM) of the PSF are shown in (**b**) and (**d**), respectively. [Color figure can be viewed in the online issue, which is available at wileyonlinelibrary.com.]

Statistical Analysis

Statistical significance (P-value) of the measurements attained in this study was evaluated using the unpaired Student's t-test with two-tailed distribution. A standard threshold ($P = 0.05$) was chosen to define statistical significance in this study.

RESULTS

Signal Response and TE Optimization

The signal response in the short-T_2 imaging to T_2 times is shown in Figure 2. For the short-T_2 component in a typical range of 0.7–6 ms in human brain (45), the signal response $\delta_{b,S}$ is nearly flat (Fig. 2a), with a gain of $g = 0.61 \pm 0.07$ (mean ± SD) relative to the intensity of the short-T_2 component at $TE_1/TE_2 = 0.5/5$ ms. For the long-T_2 component in a typical range of 16–30 ms (45), the signal response $\delta_{b,L}$ is also nearly flat (Fig. 2b) with a gain of $g = 0.18 \pm 0.03$ relative to the intensity of the long-T_2 component, showing a uniform suppression of the long-T_2 signal. For a combination of the short- and long-T_2 components (i.e., $\delta_b = 0.6\delta_{b,S} + 0.4\delta_{b,L}$), the signal response δ_b is closer to a flat one (Figs. 2c, d), with a gain of $g = 0.76 \pm 0.07$ relative to the intensity of the short-T_2 component. Consequently, optimal TEs for achieving a flat signal response are $TE_1 = 0.5$ ms and $TE_2 = 5$–6 ms. In this study $TE_2 = 5$ ms was chosen for minimizing T_2^* decay.

In contrast, signal response in TQF imaging shows much larger variation (>30%) with T_2 times: $g = 0.32 \pm 0.16$ relative to the intensity of either short- or long-T_2 component at the low end of $T_{22} = 16$ ms, but $g = 0.49 \pm 0.15$ at the high end of $T_{22} = 30$ ms (Figs. 2e, f).

Image Blurring of the Short-T_2 Component

When the TPI acquisitions were performed on a sample of bi-component relaxation, the point spread function (PSF) was dominated by the long T_2^* component

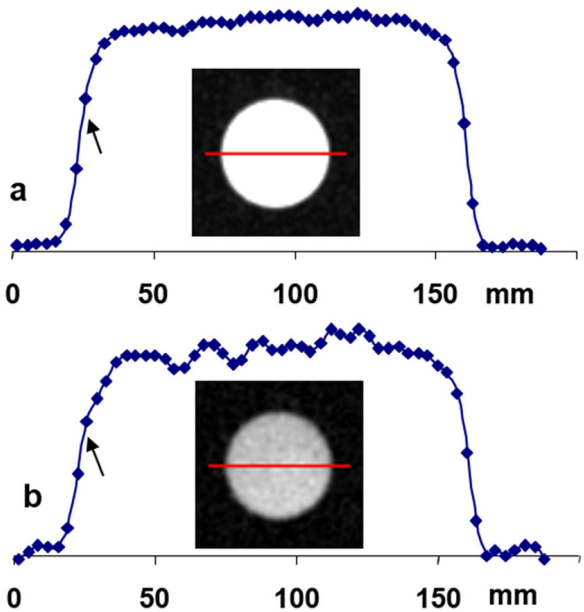

FIG. 4. Sodium images of the agarose phantom and intensity profiles throughout the diameters (red lines). **a:** SQ image at TE_1 of a measured resolution of 6.0 mm (arrow) or 1.75 pixels. **b:** ST2 image of a measured resolution of 11.35 mm (arrow) or 3.30 pixels. [Color figure can be viewed in the online issue, which is available at wileyonlinelibrary.com.]

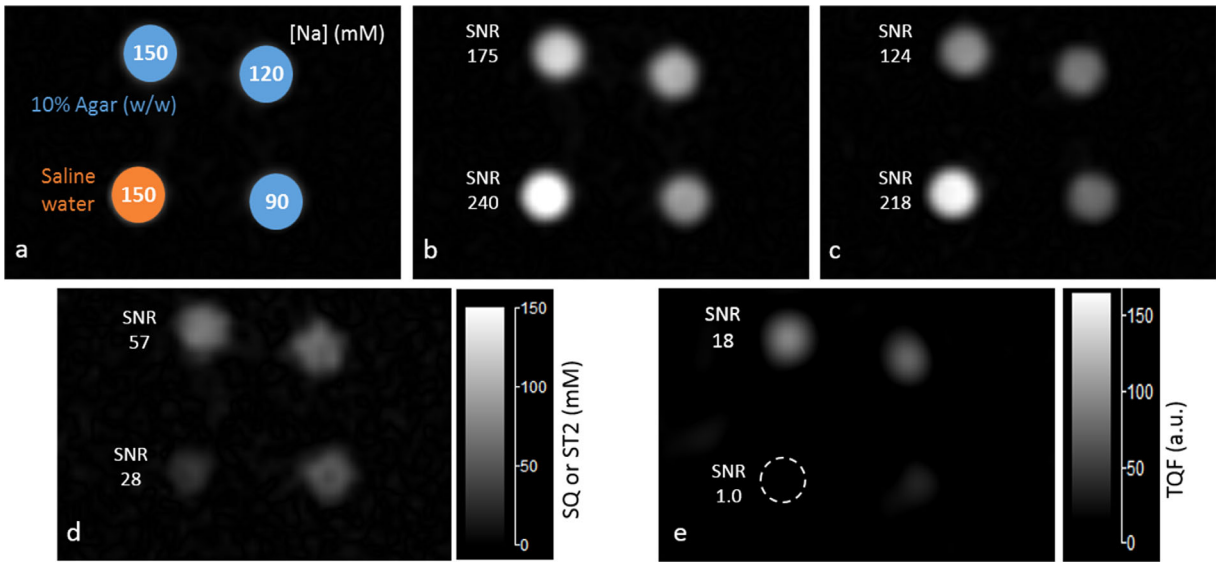

FIG. 5. Sodium images of the agar tube phantoms. **a:** Four tube phantoms: one filled with saline water of 150 mM NaCl and the other three filled with 10% w/w agar gels of 150, 120, and 90 mM NaCl, respectively. **b:** Single-quantum (SQ) image at $TE_1 = 0.5$ ms. **c:** SQ image at $TE_2 = 5$ ms. **d:** Short-T_2 (ST2) image from the subtraction between (b) and (c). **e:** Triple-quantum filtered (TQF) image of a nominal resolution 4 times lower than in the ST2 image in d. Image intensities in b–d were calibrated to sodium concentration. The measured SNR in b–e shows advantages of the short-T_2 imaging over conventional TQF imaging in SNR and resolution. [Color figure can be viewed in the online issue, which is available at wileyonlinelibrary.com.]

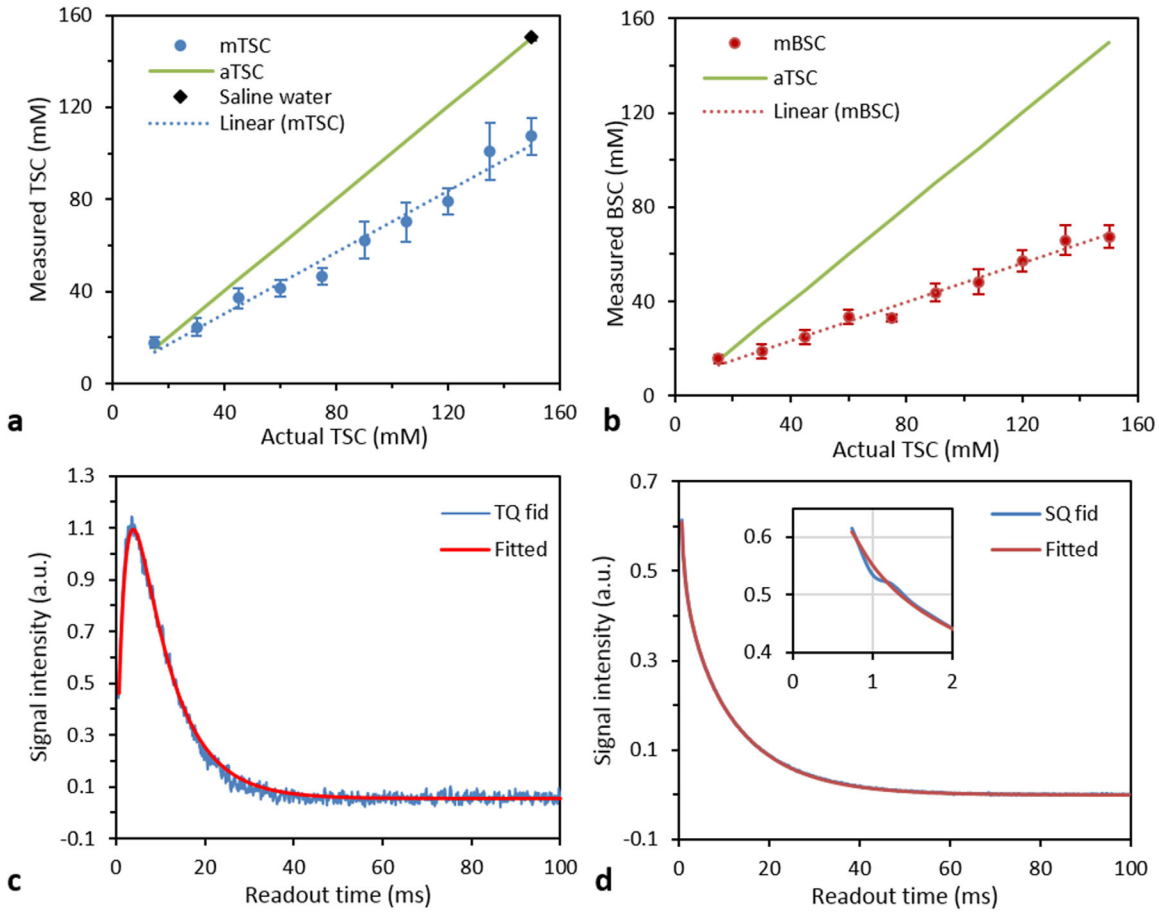

FIG. 6. Quantification on the agar tube phantoms: total sodium concentration (TSC) quantified on the SQ images at TE_1 (for the linear fitting: mTSC = 0.6681*aTSC+3.5952, $R^2 = 0.9777$) (**a**), bound sodium concentration (BSC) quantified on the ST2 images (for the linear fitting: mBSC = 0.4095*aTSC+7.0248, $R^2 = 0.9838$) (**b**), TQF fid signal of the agar tubes showing existence of the bound sodium [for the fitting curve: $T_2^* = (2.0, 8.4)$ ms, $R^2 = 0.9925$, and fitting model $s(t) = A^*(exp(-t/T_{2L}^*) - exp(-t/T_{2S}^*))$ (**c**), and SQ fid signal of the agar tubes showing that all the sodium ions in the agar gels were bound [for the fitting curve: $T_2^* = (2.8, 12.6)$ ms, $a = (57.5, 42.5)\%$, $R^2 = 0.9995$] (**d**), when compared with free sodium in the saline water which showed a much larger T_2^* of 37.0 ms in this study. [Color figure can be viewed in the online issue, which is available at wileyonlinelibrary.com.]

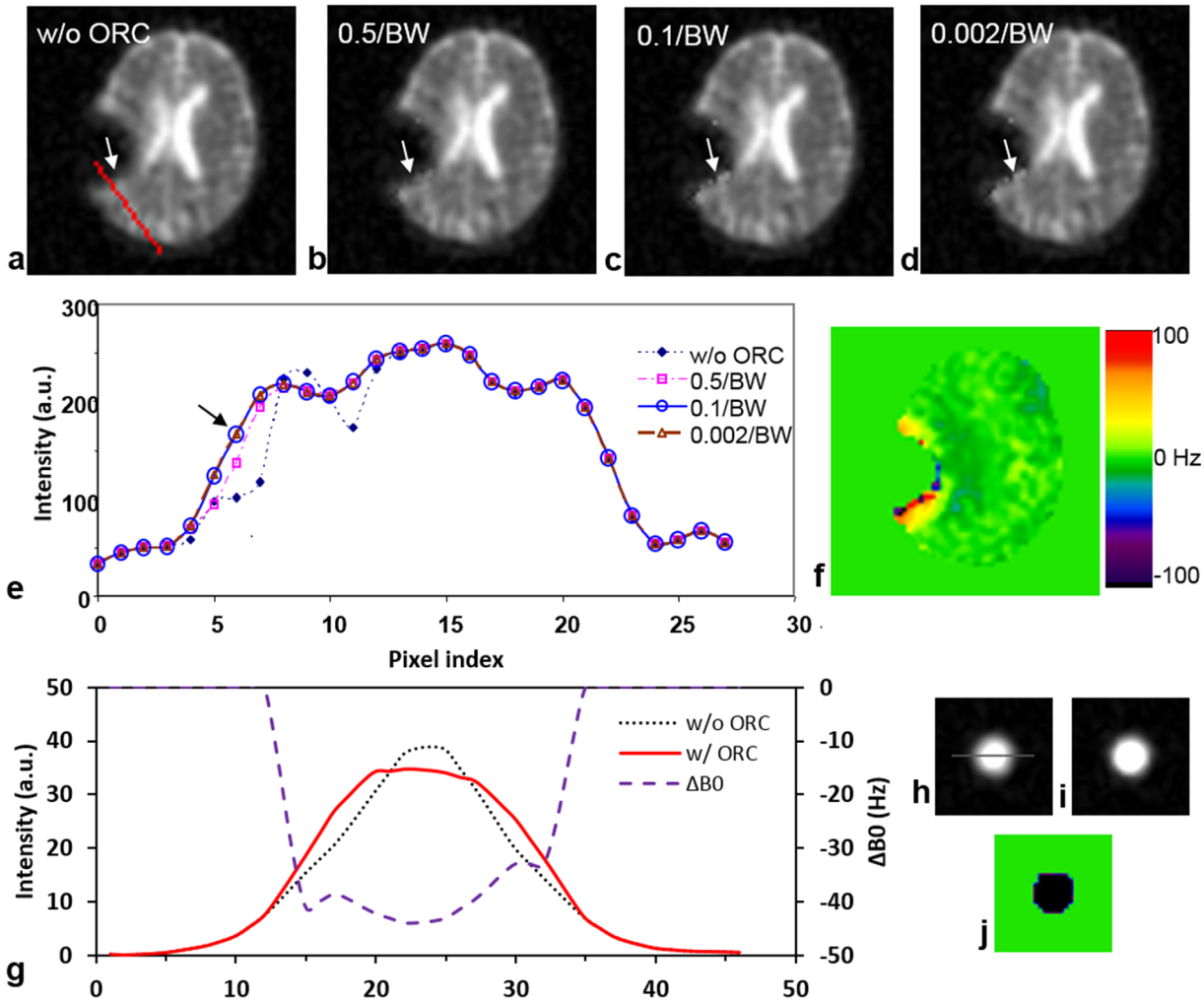

FIG. 7. Off-resonance correction (ORC) by the conjugate phase algorithm: without ORC (**a**), with ORC at a time step of 0.5, 0.1, or 0.002 periods of frequency bandwidth (BW) (**b–d**), intensity profiles along the red line in a (**e**), and a masked B_0-field map for the ORC (**f**). A smaller time step produced better ORC (arrows in a–e). The time step of 0.1/BW (or 0.5 ms or 50 data points) was as good as the time step of 0.002/BW (0.01 ms or 1 data point) for the ORC (arrow in e). **g–j**: ORC (0.5 ms in time step) on the tube phantom of saline water at 150 mM NaCl, showing recovery of the flat intensity within the tube which has a frequency offset of −40 Hz: intensity profiles along the line as shown in h (**g**), image of the tube phantom before ORC (**h**), image after ORC (**i**), and B0-field map used for the ORC (**j**). [Color figure can be viewed in the online issue, which is available at wileyonlinelibrary.com.]

(Fig. 3a). When on a sample of single-component relaxation, the PSF doubled its full width at half maximum (FWHM) for the short T_2^* component, compared with the long T_2^* component (Fig. 3c). These results suggest that image blurring for short T_2^* components is two times larger than for long T_2^* components (Fig. 3d). The larger blurring also caused spreading of energy and reduced PSF amplitude, such as 0.02 versus 0.40 at $T_2^* = 2$ ms versus 20 ms (Fig. 3b). It is worth mentioning that the subtraction of PSFs at TE_1 and TE_2 is still a single-peak, rather than two-peak, function because both PSFs share the same shape (but have different amplitude).

Image blurring (or spatial resolution) of the short-T_2 imaging was measured on the cylindrical agarose phantom in Figure 4. A profile along the diameter reflects radial symmetry, as shown in the inset images. At the left side of the profiles, the measured resolution was 1.75 pixels (or 6.02 mm) for the SQ-image at TE_1 (Fig. 4a), and 3.30 pixels (or 11.35 mm) for the short-T_2 sodium image (Fig. 4b). These measurements are in good agreement with those predicted by the TPI's PSF in Figure 3d.

Imaging on Phantoms

The short-T_2 imaging and TQF imaging on a group of tube phantoms are shown in Figure 5. To reduce noise, the TQF image was reconstructed with a smaller k-space filter of 1/4 width for the SQ images. As expected, the short-T_2 image clearly shows the four tubes and the TQF imaging completely suppressed the signal from the saline water (Fig. 5e). In contrast, the short-T_2 imaging did not completely suppress the saline water signal as significant residual signals remain (Fig. 5d).

Quantification on Phantoms

Figure 6 shows the quantification of both total and bound sodium concentrations on the SQ and short-T_2

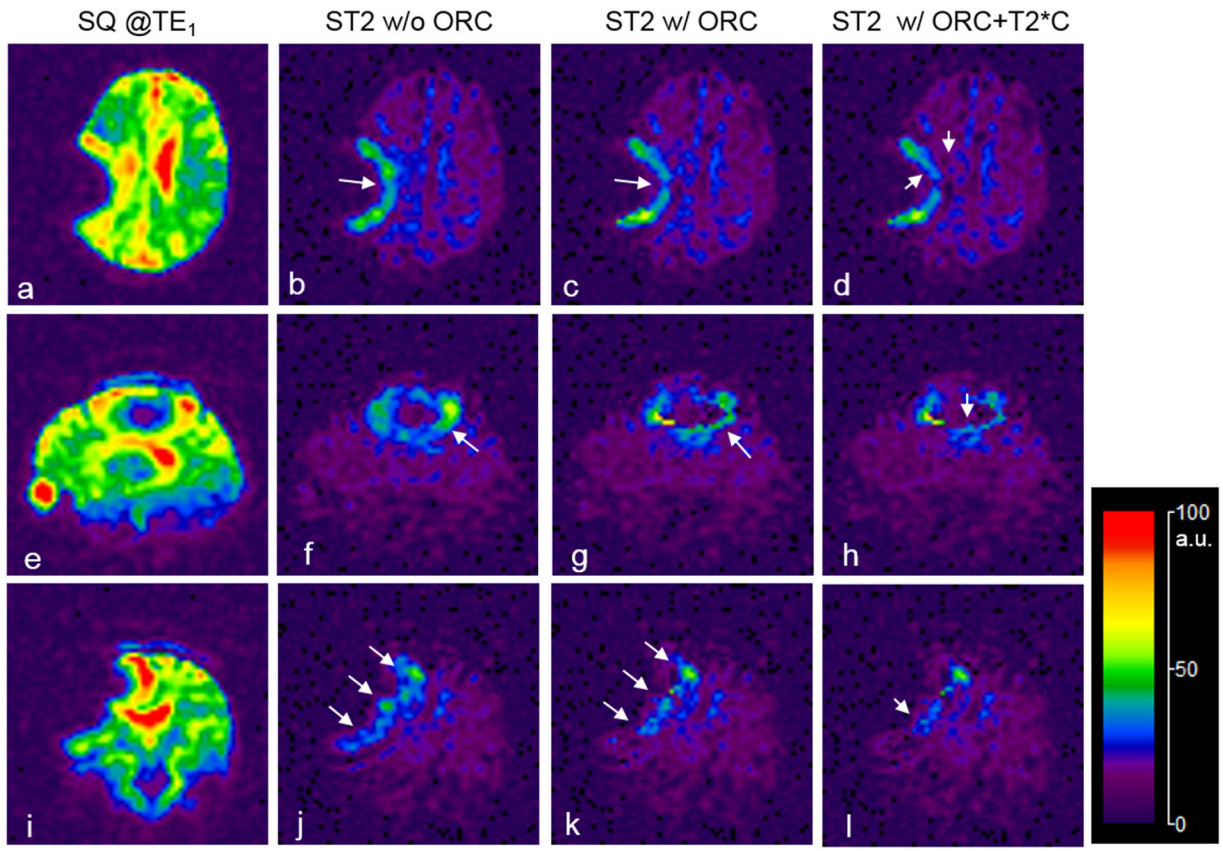

FIG. 8. Off-resonance correction (ORC) and T_2^* correction (T2*C) for the short-T_2 (ST2) image of a pediatric brain tumor patient, with the SQ images **(a, e, i)** as reference. The ST2 images were produced without ORC **(b, f, j)**, with ORC **(c, g, k)**, or with both ORC and T2*C **(d, h, l)**. While the ORC minimized image blurring (long arrows in c, g, k), the T2*C reduced image intensity as expected (short arrows in d, h, l). [Color figure can be viewed in the online issue, which is available at wileyonlinelibrary.com.]

images, respectively. The spatial variation of coil sensitivity was measured relative to the location of the saline water tube by switching the 150 mM agar tube at these locations. The relative coil sensitivity was found as (0.95, 1.0; 1.0, 1.06), fairly uniform at the locations investigated. A linear relationship between the measured and actual sodium concentrations was well established ($R^2 = 0.98$) on both images (Figs. 6a, b), although they had a different line slop due to the difference in image resolution. These linear relations demonstrate that quantification of bound sodium on short-T_2 images is feasible. The binding of total sodium in the agar phantoms was confirmed by the FID signals for the SQ and TQF imaging (Figs. 6c, d).

Human Brain Imaging: Off-Resonance Correction

Several time steps were investigated to find an optimal value for the time step. Figure 7 shows an example of the off-resonance correction in a worst case of pediatric patient where large off-resonance frequencies (40–100 Hz, Fig. 7e) appear around a programmable Silastic shunt (Medtronic, Minneapolis, MN) implanted in the brain. The intensity profiles across the region (Fig. 7f) shows the improvement in the off-resonance correction when reducing the time step from 0.5 to 0.1 periods of the frequency bandwidth (BW) in the B_0-field map. However, further reducing time step from 0.1 to 0.002/BW (i.e., single data point) did not further improve the correction. Consequently, the time step of 0.1/BW (or 0.5 ms) was used in this study to reduce total computation time. The study on a uniform tube phantom confirmed the effectiveness of the ORC correction (Figs. 7g–j). The computation time for a single time step was 1.644 s on our network server of eight node Linux CPU cluster with 16 Intel Xeon E5–2667 2.90 GHz six-core processors. This led to total ORC computing time of 2.0 min in this study at a time step of 0.5 ms or 50 data points, or otherwise 100 min at a time step of single data point.

Human Brain Imaging: T_2^* Correction

The T_2^* correction was implemented on the TE_2 images after the off-resonance correction. The B_0-field map for the T_2^* correction was estimated on the off-resonance corrected SQ images. Figure 8 demonstrates a T_2^* correction on the short-T_2 images. While the ORC reduced artifacts in the background of short-T_2 images (Figs. 8c, g, k), the T_2^* correction reduced intensity of the residual artifacts as shown in Figures 8d, h, l.

Human Brain Imaging: Quantification of TSC and vBSC

Quantification of total and volume-fraction weighted bound sodium concentrations was implemented on both

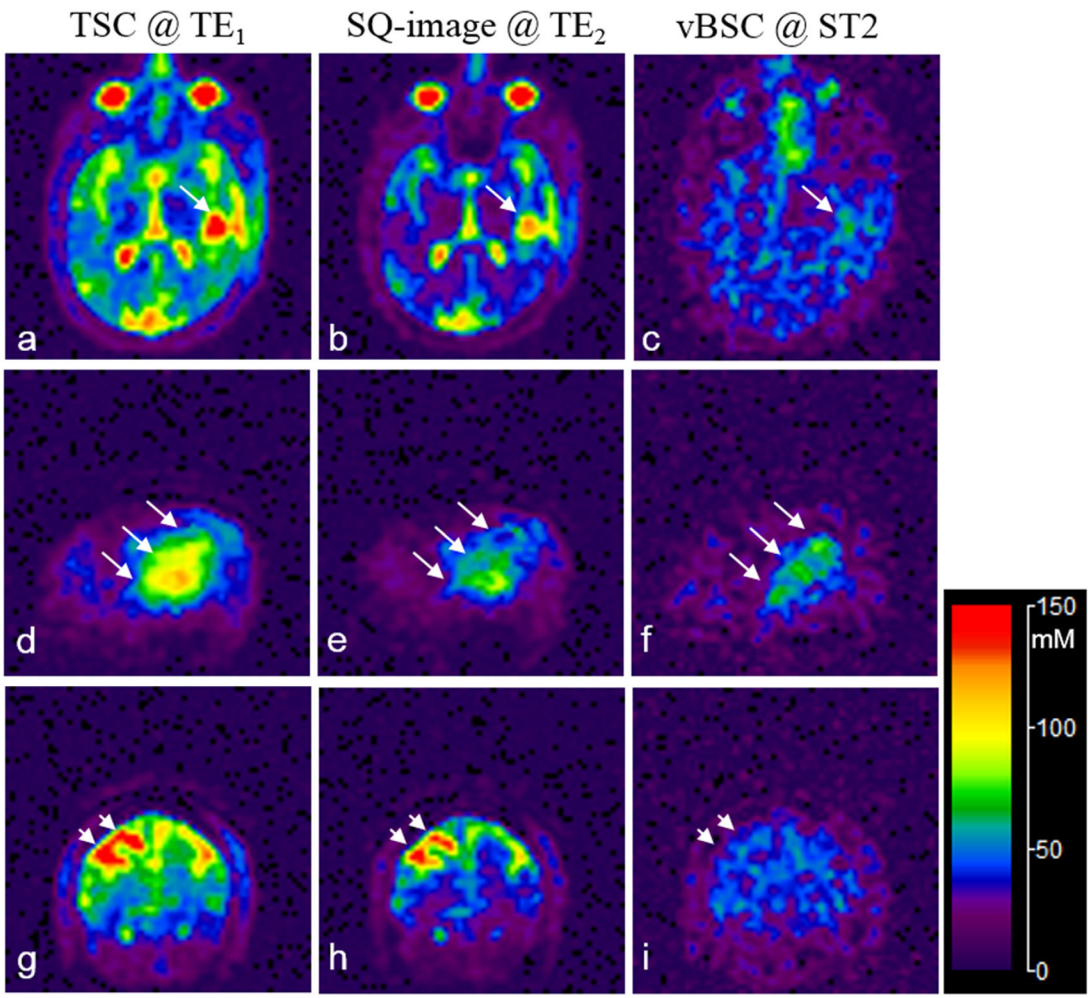

FIG. 9. Sodium images of quantified total sodium concentration (TSC) and volume-fraction weighted bound sodium concentration (vBSC) for an adult brain tumor patient: transverse (**a–c**), sagittal (**d–f**), and coronal (**g–i**) views. The tumor region (long arrows, d–f) shows an increase not only in TSC (a,d) but also in vBSC (c,f). The CSF-filled cavity (short arrows, g–i) shows an increase in TSC (g) but not in vBSC (i). The calibrated SQ-images (b, e, h) at TE_2 (=5.0 ms) show visible decays in intensity of the short-T_2 component compared with the corresponding images (a, d, g) at TE_1 (=0.44 ms). The tumor and cavity was confirmed in the proton (^{1}H) images in Fig. 10.

SQ- and short-T_2 images after the off-resonance and T_2^* corrections. Figure 9 demonstrates an example from an adult brain tumor patient with glioblastoma before anticancer treatment. The tumor region was confirmed by the proton MR images in Figure 10, showing enhancement on both contrast-enhanced T_1-weighted (CE-T1w) image and fluid attenuated inversion recovery (FLAIR) image. The sodium SNR is 39.7 in the CSF region on the SQ-image at TE_1, and 15.3 in the tumor region on the short-T_2 image, compared with 4.2 outside the tumor region (sagittal, Figure 9f). The tumor region has TSC of 86.7 ± 13.5 mM (mean $\pm$ SD) and vBSC of 59.6 ± 11.3 mM. The vBSC value is 3.6 times ($P < 0.0001$) higher than outside the tumor region where vBSC $= 16.6 \pm 11.1$ mM. The variance in the TSC or vBSC value reflects inhomogeneity in the tumor/nontumor regions measured, rather than the noise-related variance which is much smaller. For instance, vBSC is 25.9 ± 1.2 mM in a region of normal gray matter outside the tumor.

DISCUSSION

The short-T_2 sodium imaging, which is a subtraction of two single-quantum sodium images acquired at different TEs, has been demonstrated as an alternative to triple-quantum filtered imaging for measurement of bound sodium concentration in the brain. The key point in this method is that subtraction between the two SQ-images highlights signals from short-T_2 relaxation while suppresses signals from long-T_2 relaxation. The short-T_2 relaxation originates from bound sodium of bi-exponential decay. The bound sodium mainly exists in intracellular space in the brain and thus is of interest for monitoring early response of cancer cells to therapies in brain tumor patients. Major advantages of the short-T_2 imaging over TQF imaging are the lower SAR production (single versus triple RF pulses), the shorter scan time (20 versus 40 min), and the higher SNR (6 versus 1) or higher spatial resolution. However, the subtraction also raises challenges such as B_0-field inhomogeneity induced off-resonance artifacts, T_2^*-related fluctuation of

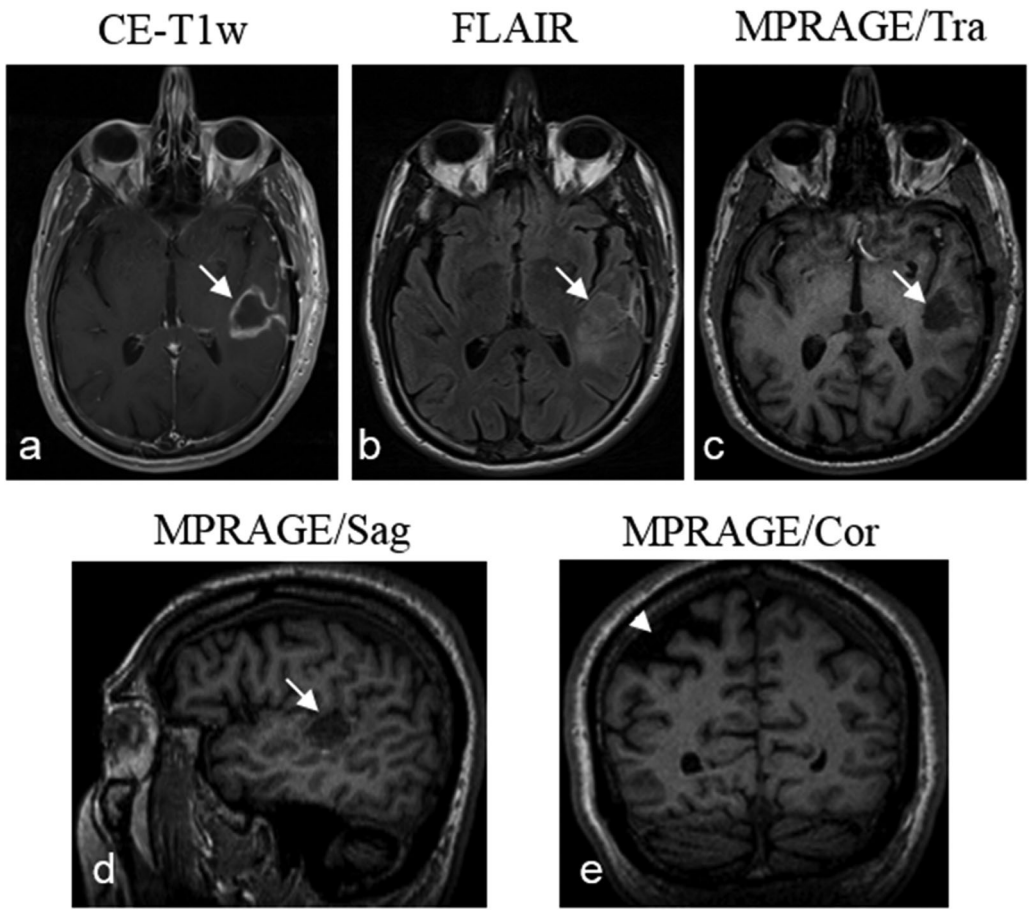

FIG. 10. Proton (^{1}H) MR images of the same patient as shown in Figure 9 for confirming the tumor (arrows) and cavity (arrowhead) in the brain. The tumor has hyperintensity in both CE-T1w (**a**) and FLAIR (**b**) images, but has hypointensity in the MPRAGE image in transverse or sagittal view (**c,d**). **e:** The cavity has low intensity in the MPRAGE image in coronal view.

measurements across scans, and potential motion artifacts between the two TE acquisitions.

Off-resonance correction by means of the time-domain conjugate phase algorithm has been shown to be effective in minimizing image blurring around the implants (Fig. 7). This correction did not require extra scans because the B_0-field map was self-generated by the two-TE acquisitions and no registration was needed between them. However, this correction was still incomplete because large inhomogeneity of the B_0-field might not be detectable in the TE_2 image due to weak signal from areas such as the sinus regions in Figures 9a–c.

The T_2^* decay was corrected to T_2 decay in the TE_2 image by taking advantage of the spatial resolution shared by the B_0-field map and TE-images. The ultimate goal of this correction is to stabilize short-T_2 imaging across scans. However, reproducibility of the short-T_2 imaging was not investigated in this study as it required a dedicated experimental design which was beyond the scope of this study. However, it is worth mentioning that the T_2^* correction is for correcting local macroscopic, rather than microscopic, inhomogeneity of the B_0 field. Thus, the corrected TE_2 image is still T_2^*-weighted, but should be closer to the T_2-weighted and be more reproducible.

The measured spatial resolution of the short-T_2 image was 3.30 pixels (or 11.35 mm) on the large cylindrical agarose phantom (Fig. 4b), compared with 1.75 pixels (or 6.02 mm) in the corresponding SQ-image (Fig. 4a). This resolution is specific to the scheme of TPI acquisitions used in this study. It is possible to increase image resolution by using different parameters in the TPI trajectory (38) or by using different schemes for data acquisition at a cost of reduced SNR, such as the acquisition-weighted stack of spirals (AWSOS) (40) and others (41).

Motion may exist between the two TE images as the time gap between the two TE scans is long (~10 min). Motion correction may be needed for the TE_2 image if it is visually detectable. In this study there was no visible motion detected. In the future, an interleaved acquisition at TE_1 and TE_2, or a double-TE acquisitions per RF excitation, may be used to minimize the motion.

Quantification for total and bound sodium concentrations can be implemented in the short-T_2 imaging simultaneously. TSC and vBSC share the same internal calibration for quantification. This eliminates the need for a separate calibration for vBSC and simplifies imaging procedures in clinical setting. This unique feature stems from the short-T_2 images sharing the same signal scale with the SQ images. In contrast, TQF images have

completely different signal scale from corresponding SQ images and are not suitable for quantification of bound sodium.

A major drawback of the short-T_2 imaging is the incomplete suppression of long T_2 signal (Fig. 5d). This restricts its application to high concentrations (>45 mM) of bound or intracellular sodium (Fig. 6), such as cancer cells and injured/damaged cells. Bound sodium at low concentrations will join the free sodium in the background of the short-T_2 image.

Further improvements for the short-T_2 imaging are needed. First, the spatial resolution needs to be increased at least as high as that for the SQ imaging. This may be achieved by using shorter readout time which in turn reduces SNR unfortunately. Increasing SNR is thus the key issue. Multi-channel receiver array has the potential to increase SNR by a factor of 2.0 (46). The higher field strength such as 7 Tesla has the potential to double SNR over the 3T field. A combination of both strategies holds great promise to address the resolution issue. Second, motion between the two TE acquisitions need to be minimized. This may be realized by alternating TE acquisitions in a single scan, or by performing two TE acquisitions in one RF excitation.

CONCLUSIONS

The proposed short-T_2 sodium imaging has been demonstrated through phantom and human studies at 3T as a feasible approach to quantification of bi-exponential (or bound) sodium. It has advantages over triple-quantum filtered imaging, such as low SAR, short acquisition time, and high SNR and resolution. It has limitations as well, such as residual long-T_2 signal. This restricts its application to large changes in concentration (>45 mM) of bound or intracellular sodium in the brain, such as in cancer cells, injured cells or degenerative neurons. Nevertheless, the short-T_2 sodium imaging may have substantial use in nonsurgical treatment monitoring of both pediatric and adult brain tumors and in detection of neurological disorders caused by nerve cell injury, damage or degeneration.

ACKNOWLEDGMENTS

The authors thank Dr. Tiejun Zhao at MR R&D Collaborations (Pittsburgh, PA), Siemens Healthcare USA for his helpful discussions on the work described in this study. Y.Q., C.M.L., J.D., F.S.L., and J.M.M. were funded in part by NIH, A.P., and V.K.L. by Children's Hospital of Pittsburgh Foundation and Ian's Friends Foundation, and Y.Q. by the Department of Radiology Development Fund, University of Pittsburgh.

REFERENCES

1. Cope F. NMR evidence for complexing of Na+ in muscle, kidney, and brain, and by actomyosin. The relation of cellular complexing of Na+ to water structure and to transport kinetics. J Gen Physiol 1967; 50:1353–1375.
2. Shinar H, Navon G. NMR relaxation studies of intracellular Na+ in red blood cells. Biophys Chem 1984;20:275–283.
3. Gupta RK, Gupta P. Direct observation of resolved resonances from intra- and extracellular sodium-23 ions in NMR studies of intact cells and tissues using dysprosium(III)tripoly-phosphate as a paramagnetic shift reagent. J Magn Reson 1982;47:344–350.
4. Borthakur A, Shapiro EM, Beers J, Kudchodkar S, Kneeland JB, Reddy R. Effect of IL-1β-induced macromolecular depletion on residual quadrupolar interaction in articular cartilage. J Magn Reson Imaging 2002;15:315–323.
5. Eliav U, Shinar H, Navon G. The formation of a second-rank tensor in 23Na double-quantum-filtered NMR as an indicator for order in a biological tissue. J Magn Reson 1992;98:223–229.
6. Thulborn KR, Davis D, Adams H, Gindin T, Zhou J. Quantitative tissue sodium concentration mapping of the growth of focal cerebral tumors with sodium magnetic resonance imaging. Magn Reson Med 1999;41:351–359.
7. Cameron IL, Smith NK, Pool TB, Sparks RL. Intracellular concentration of sodium and other elements as related to mitogenesis and oncogenesis in vivo. Cancer Res 1980;40:1493–1500.
8. Hubbard, PS. Nonexponential nuclear magnetic relaxation by quadrupole interactions. J Chem Phys 1970;53:985–987.
9. Shporer M, Civan MM. Nuclear magnetic resonance of sodium-23 linoleate-water. Biophys J 1972;12:114–122.
10. Berendsen HJC, Edzes HT. Observation and general interpretation of sodium magnetic resonance in biological material. Ann N Y Acad Sci 1973;204:459–480.
11. Andrasko J. Nonexponential relaxation of 23Na+ in agarose gels. J Magn Reson 1974;16:502–504.
12. Cohen BL. Concepts of nuclear physics. New York: McGraw-Hill; 1971. 435 p.
13. Joffe J, Urey HC. The spin of the sodium nucleus. Phys Rev 1933;43: 761.
14. Jaccard G, Wimperis S, Bodenhausen G. Multiple-quantum NMR spectroscopy of S=3/2 spins in isotropic phase: a new probe for multiexponential relaxation. J Chem Phys 1986;85:6282–6293.
15. Pekar J, Leigh JS. Detection of biexponential relaxation in sodium-23 facilitated by double-quantum filtering. J Magn Reson 1986;69:582–584.
16. Bull TE. Nuclear magnetic relaxation of spin-3/2 nuclei involved in chemical exchange. J Magn Reson 1972;8:344–353.
17. Reddy R, Shinnar M, Wang Z, Leigh JS. Multiple-quantum filters of spin-3/2 with pulses of arbitrary flip angle. J Magn Reson 1994;104: 148–152.
18. Bax A, de Jong PG, Mehlkopf AF, Smidt J. Separation of the different orders of NMR multiple-quantum transitions by the use of pulsed filed gradients. Chem Phys Lett 1980;69:567–570.
19. Chung C, Wimperis S. Optimum detection of spin-3/2 biexponential relaxation using multiple-quantum filteration techniques. J Magn Reson 1990;88:440–447.
20. Hancu I, Boada FE, Shen GX. Three-dimensional triple-quantum-filtered 23Na imaging of in vivo human brain. Magn Reson Med 1999;42:1146–1154.
21. Tsang A, Stobbe RW, Beaulieu C. Triple-quantum-filtered sodium imaging of the human brain at 4.7T. Magn Reson Med 2012;67:1633–1643.
22. Navon G. Complete elimination of the extracellular 23Na NMR signal in triple quantum filtered spectra of rat heart in the presence of shift reagents. Magn Reson Med 1993;30:503–506.
23. Allis JL, Seymour AL, Radda GK. Absolute quantification of intracellular Na+ using triple-quantum-filtered sodium-23 NMR. J Magn Reson 1991;93:71–76.
24. Kline RP, Wu EX, Petrylak DP, Szabolcs M, Alderson PO, Weisfeldt ML, Cannon P, Katz J. Rapid in vivo monitoring of chemotherapeutic response using weighted sodium magnetic resonance imaging. Clin Cancer Res 2000;6:2146–2156.
25. Ouwerkerk R, Bleich KB, Gillen JS, Pomper MG, Bottomley PA. Tissue sodium concentration in human brain tumors as measured with 23Na MR imaging. Radiology 2003;227:529–537.
26. Stobbe R, Beaulieu C. In vivo sodium magnetic resonance imaging of the human brain using soft inversion recovery fluid attenuation. Magn Reson Med 2005;54:1305–1310.
27. Rong P, Regatte RR, Jerschow A. Clean demarcation of cartilage tissue 23Na by inversion recovery. J Magn Reson 2008;193:207–209.
28. Benkhedah N, Bachert P, Semmler W, Nagel AM. Three-dimensional biexponential weighted 23Na imaging of the human brain with higher SNR and shorter acquisition time. Magn Reson Med 2013;70: 754–765.
29. Benkhedah N, Bachert P, Nagel AM. Two-pulse biexponential-weighted 23Na imaging. J Magn Reson 2014;240:67–76.

30. Haacke EM, Brown RW, Thompson MR, Venkatesan R. Magnetic resonance imaging–physical principles and sequence design. New York: John Wiley & Sons; 1999. 914 p.
31. Hilal SK, Maudsley AA, Ra JB, Simon HE, Roschmann P, Wittekoek, Cho ZH, Mun SK. In vivo NMR imaging of sodium-23 in the human head. J Comput Assist Tomogr 1985;9:1–7.
32. Ra JB, Hilal SK, Oh CH. An algorithm for MR imaging of the short T2 fraction of sodium using the FID signal. J Comput Assist Tomogr 1989;13:302–309.
33. Perman WH, Thomasson DM, Bernstein MA, Turski PA. Multiple short-echo (2.5ms) quantitation of in vivo sodium T2 relaxation. Magn Reson Med 1989;9:153–160.
34. Batha R, Menon RS. Long component time constant of 23Na T2* relaxation in healthy human brain. Magn Reson Med 2004;52:407–410.
35. Harrington MG, Salomon RM, Pogoda JM, Oborina E, Okey N, Johnson B, Schmidt D, Fonteh AN, Dalleska NF. Cerebrospinal fluid sodium rhythms. Cerebrospinal Fluid Res 2010;7:3.
36. Noll DC, Fessler JA, Sutton BP. Conjugate phase MRI reconstruction with spatially variant sample density correction. IEEE Trans Med Imaging 2005;24:325–336.
37. Sutton BP, Noll DC, Fessler JA. Fast, iterative image reconstruction for MRI in the presence of field inhomogeneities. IEEE Trans Med Imaging 2003;22:178–188.
38. Boada FE, Gillen JS, Shen GX, Chang SY, Thulborn KR. Fast three dimensional sodium imaging. Magn Reson Med 1997;37:706–715.
39. Fiege DP, Romanzetti S, Mirkes CC, Brenner D, Shah NJ. Simultaneous single-quantum and triple-quantum-filtered MRI of 23Na (SISTINA). Magn Reson Med 2013;69:1691–1696.
40. Qian Y, Zhao T, Zheng H, Weimer J, Boada FE. High-resolution sodium imaging of human brain at 7 T. Magn Reson Med 2012;68:227–233.
41. Rahmer J, Börnert P, Groen J, Bos C. Three-dimensional radial ultrashort echo-time imaging with T2 adapted sampling. Magn Reson Med 2006;55:1075–1082.
42. Nagel AM, Laun FB, Weber MA, Matthies C, Semmler W, Schad LR. Sodium MRI using a density-adapted 3D radial acquisition technique. Magn Reson Med 2009;62:1565–1573.
43. Atkinson IC, Lu A, Thulborn KR. Clinically constrained optimization of flexTPI acquisition parameters for the tissue sodium concentration. Magn Reson Med 2011;66:1089–1099.
44. Gudbjartsson H, Patz S. The Rician distribution of noisy MRI data. Magn Reson Med 1995;34:910–914. Erratum in Magn Reson Med 1996;36:332.
45. Ra JB, Hilal SK, Cho ZH. A method for in vivo MR imaging of the short T2 component of sodium-23. Magn Reson Med 1986;3:296–302.
46. Qian Y, Zhao T, Wiggings GC, Wald LL, Zheng H, Weimer J, Boada FE. Sodium imaging of human brain at 7T with 15-channel array coil. Magn Reson Med 2012;68:1807–1814.